

# Strength and Phase Identification of Autogenous Laser Brazed Dissimilar Metal Microjoints

**Gen Satoh**

Manufacturing Research Lab,  
Columbia University,  
New York, NY 10027

**Caian Qiu**

Champaign Simulation Center,  
Caterpillar,  
Champaign, IL 61820

**Syed Naveed**

Boston Scientific Corporation,  
Marlborough, MA 01752

**Y. Lawrence Yao**

Manufacturing Research Lab,  
Columbia University,  
New York, NY 10027

*The continued advancement of implantable medical devices has resulted in the need to join a variety of dissimilar, biocompatible metal pairs to enable selective use of their unique properties. Typical materials used in implantable medical devices include stainless steel (SS), titanium, platinum (Pt), as well as shape memory materials such as NiTi. Joining these dissimilar metal pairs, however, often results in excessive formation of brittle intermetallics, which significantly reduce the strength of the joints. The use of filler materials to combat the formation of intermetallics, however, results in reduced biocompatibility. Autogenous laser brazing is a novel process that is able to form thin, localized joints between dissimilar metal pairs without filler materials. In this study, the formation of autogenous laser brazed joints between NiTi and SS wires is investigated through experiments and numerical simulations. The strength, composition, microstructure, and phase formation of the resultant joints are investigated as a function of processing parameters and thermal, fluid flow, and phase prediction simulations are used to aid in understanding the joint formation mechanism. [DOI: 10.1115/1.4028778]*

## Introduction

The joining of dissimilar materials is a critical issue in the continued development of advanced medical devices due to the unique properties possessed by materials such as NiTi, Pt, and SS, among others. Requirements for joining of dissimilar biocompatible materials can stem from introducing unique functionalities through the use of shape memory alloys (SMAs) such as NiTi in conjunction with SS, or for decreasing costs while maintaining exceptional corrosion resistance in Pt-to-SS joints. To address these requirements, a new laser joining process is investigated to form autogenous (no filler material) joints between dissimilar, biocompatible metal pairs. The autogenous laser joining process would enable seamless joining of these components and eliminate the need for proprietary adhesives and filler materials used in many current designs.

Laser-based joining processes, due to their low thermal input and small spot size, have become the primary joining mechanism of metallic parts in medical devices such as pacemakers and implantable cardioverter defibrillators. The advantages of lasers in joining processes over conventional heat sources, such as minimal heat-affected zones and controlled energy delivery, are vital to medical device manufacturing processes due to the thermal sensitivity of components as well as their continued miniaturization. These same characteristics are crucial in forming reliable joints between dissimilar materials. The tightly controlled heat input allows precise, selective processing and strict control over the melting and intermixing of the two materials.

Of the limited number of metals identified as proven or potential biocompatible materials, NiTi and SS have received particular attention for use in medical devices. SS enables physically robust bulk implants and devices with exceptional biocompatibilities at relatively low cost. Smart materials such as SMAs make possible novel device functionalities through thermally driven actuation and superelastic deformation. The shape memory and superelastic

effects of SMAs have been used in medical devices for steerable catheters and stents but are generally limited to monolithic components and suffer from limited radiopacity [1]. Joining different biocompatible material pairs can help to alleviate some of the issues faced by single materials. The ability to form a robust joint between NiTi and SS would enable the incorporation of unique device functionalities (shape memory materials) in low cost medical devices.

Dissimilar metal joints, however, are often complicated by the formation of new phases such as brittle intermetallics within the joint that lead to low strength and premature failure. These phases are typically formed when the two base materials are allowed to mix and result in undesirable mechanical properties. A number of processes have been investigated for joining dissimilar material pairs that form brittle intermetallic phases. Traditional joining processes have limited spatial selectivity and large heat inputs (arc welding, etc.), which promote excessive brittle phase formation. Brazing, which utilizes a filler material with a lower melting temperature than either of the base materials, eliminates melting of the base metals and can potentially avoid intermetallic formation but requires careful selection of the filler material. This is particularly difficult in medical devices due to the required biocompatibility. Li et al. have investigated the laser brazing of NiTi-SMAs to SS using silver-based filler materials but found that the corrosion resistance of the joint was worse than that of the base materials [2].

Solid-state processes can also be performed, which allows for greater control over material mixing. One such process, diffusion bonding, has been investigated for direct bonding of biocompatible material pairs such as NiTi/SS by Ghosh and Chatterjee [3]; however, the formation of brittle intermetallics could not be prevented. Kundu et al. [4,5] performed diffusion bonding of the same material pair using Ni and Cu interlayers but also observed the formation of intermetallics at the joint interfaces. In addition, this bonding process requires heating of the entire device to elevated temperatures and, like ultrasonic welding, the ability to impart a compressive stress on the joint. These requirements make such process difficult for medical devices with heat-sensitive components, small size, and complex joint geometries.

Contributed by the Manufacturing Engineering Division of ASME for publication in the JOURNAL OF MANUFACTURING SCIENCE AND ENGINEERING. Manuscript received January 26, 2014; final manuscript received September 17, 2014; published online November 26, 2014. Assoc. Editor: Wei Li.

Intermetallic-free dissimilar metal joints have been achieved through the use of adhesives. These joints, however, are not well suited to extended implantation in the body [6].

In this study, a novel process, autogenous laser brazing, is used to join two biocompatible materials, stainless steel 316 and NiTi. The joint geometry is analyzed through optical and scanning electron microscopy (SEM) of sample cross sections while compositional analysis is performed using energy-dispersive X-ray spectroscopy (EDS). Joint strength is determined through tensile testing to fracture and fracture surface morphology is observed using SEM. Phases formed in the dissimilar metal joint are identified using a combined EDS and electron backscatter diffraction (EBSD) method.

## Background

**Autogenous Laser Brazing Process.** While the majority of laser-based joining processes use the laser input to directly melt the base or filler materials at the joint, the autogenous laser joining process aims to make the joint significantly smaller than the laser beam spot size. The joining process involves laser irradiation of one of the base materials starting some distance away from and moving toward the dissimilar metal interface. A schematic diagram of the joining process is shown in Fig. 1.

Laser parameters such as power and speed are chosen such that the equilibrium temperature of the irradiated piece does not exceed its melting temperature. Heat accumulation due to the thermal resistance of the interface causes the temperature at the interface to rise above the melting temperature of the one of the base materials as the laser beam approaches, forming a molten layer. The laser beam is turned off as the spot reaches the interface and the melt layer is quenched when it comes in contact with the adjacent cold workpiece forming an autogenous braze-like joint. The irradiation of the lower melting point material aids in the localization of the melting to the interface. In the case of a NiTi to SS joining, the NiTi, with an equilibrium melting temperature of 1310 °C compared to 1375 °C for SS, will be irradiated.

This process minimizes mixing of the two materials due to the minimal melt volume, high quench rate, and localized melting of one side of the weld joint. This process is also autogenous, eliminating the need for filler materials when joining metallurgically incompatible materials with similar melting temperatures.

**Intermetallic Phases.** One of the main impediments to the direct joining of dissimilar metals is the formation of intermetallic phases. These phases are typically highly ordered and exist within a limited homogeneity range. Due to their highly ordered and complex structures, many intermetallics have long burgers vectors, which limit plastic deformation and render them extremely brittle. The limited homogeneity range also results in the

formation of two-phase microstructures such as dendrites or eutectics unless the composition is within a specific range.

While the formation of intermetallic phases is inevitable in many dissimilar metal pairs at equilibrium, processing techniques have been developed that have shown the ability to decrease intermetallic phase formation or control their microstructures for enhanced strength. Borrisutthekul et al. [7] have shown that controlling heat flow and cooling rate through increased welding speed and the use of a high thermal conductivity heat sink can decrease the thickness of the intermetallic layer in laser welds between high-strength steel and a 6000-series aluminum alloy. Louzguine et al. [8] reported the formation of high-strength, high-ductility Ti-Fe bulk alloys, which typically form many brittle intermetallics such as TiFe and TiFe<sub>2</sub>. The results were attributed to the extended solubility of Fe in  $\beta$ -Ti due to the high quench rate as described by Ray [9]. In situ time and spatially resolved X-ray diffraction methods have been developed by Elmer and Palmer [10,11] and have been used to investigate the formation of phases during welding of Ti-6Al-4V to medium carbon steel dissimilar metal pairs.

Control over the material mixing within dissimilar metal joints has also been investigated for limiting intermetallic phase formation. Borrisutthekul et al. [12] utilized a specific edge-line lap welding geometry to minimize penetration of the weld pool to the lower plate in laser fusion welding of magnesium and aluminum alloy plates. The effect of interlayers with various compositions for joining Ti and SS was investigated by Lee et al. [13]. Several studies using laser offsets for compositional control of dissimilar metal joints have been reported by Mys and Schmidt [14] and Yao et al. [15] for copper-aluminum and copper-steel material pairs, respectively. The proposed autogenous laser brazing process is designed to minimize mixing of the dissimilar materials as well as increase the cooling rate experienced by the molten material to inhibit intermetallic phase formation while eliminating the need for additional filler materials or adhesives.

**Numerical Simulation.** The numerical simulation performed in this study aims at understanding the thermal profile resulting from the unique scanning procedure employed during autogenous laser brazing, the resultant fluid flow within the molten pool, and using that thermal profile to predict the phases, which are expected to form at the joint interface. Thermal modeling of the joining process is performed using a three-dimensional finite element code that models half of each of the wires with a symmetric boundary condition to reduce computation time. The thermal simulation is fully coupled with the fluid-flow simulation such that convective flow results in an associated heat transfer. The laser beam is modeled as a Gaussian beam traveling at a constant velocity across the top of one wire as

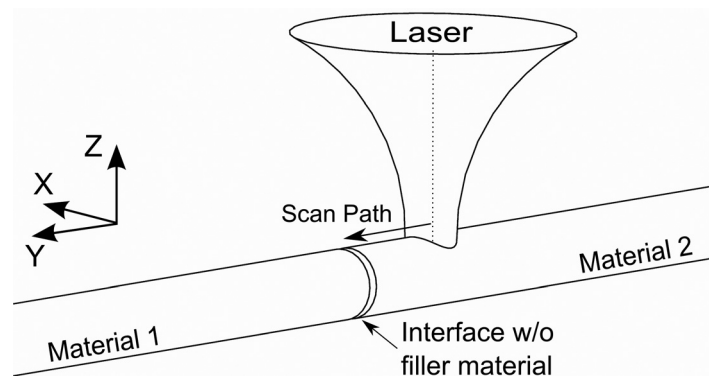


Fig. 1 Schematic diagram of proposed autogenous laser brazing process for (a) wire-wire ( $\sim 400 \mu$  in diameter). Wire-wire process utilizes a Gaussian laser intensity distribution.

$$Q = Q_{\max} - \frac{3\left((X - X_o)^2 + (Y - (Y_o + Vt))^2\right)}{R_o^2} \quad (1)$$

where  $Q$  is the flux at point  $(X, Y)$ ,  $Q_{\max}$  is the peak flux,  $R_o$  is the beam spot size,  $X_o$  and  $Y_o$  are the initial position of the laser spot,  $V$  is the scan velocity, and  $t$  is time. Thermal contact conductance across the dissimilar metal interface is modeled as a step function as a function of temperature with the contact conductance increasing from 0.1 W/m/K for solid–solid contact to 10 W/m/K, the thermal conductivity of pure NiTi, for solid–liquid contact. Solid–solid contact is the main conduction pathway during irradiation prior to the occurrence of melting and the conductance value is used as a tuning parameter for the thermal profile with the goal of achieving agreement in the resultant composition profile between the experimental results and the simulation. Solid–liquid contact occurs when the surface of the irradiated wire at the joint melts, wetting the adjacent, solid surface of the abutting wire. The contact conductance is spatially resolved over the wire–wire interface allowing for more accurate modeling of the melting phenomenon and thermal profile during processing. The maximum achieved contact conductance at each point is also considered to remain during cooling to mimic the formation of a seamless joint after processing.

A fluid-flow model was developed in conjunction with the heat transfer simulation in order to develop and understanding of the mechanism of mixing occurring within the dissimilar metal joint during processing. Fluid flow is modeled using the Navier–Stokes equations, which take as input the current thermal profile of the wire as determined through the heat transfer simulation. Fluid flow is driven by Marangoni convection due to the change in surface tension of liquids with temperature. The surface tension force is implemented as a traction force on the fluid free surface and is a function of the temperature gradient along a surface in the  $x$ -direction in the form

$$\eta \frac{du}{dy} = \gamma \frac{dT}{dx} \quad (2)$$

where  $u$  is the flow velocity,  $y$  is the direction perpendicular to the surface,  $T$  is temperature,  $\eta$  is viscosity, and  $\gamma$  is the surface tension coefficient with temperature. A positive surface tension coefficient of  $1.6 \times 10^{-4}$  N/m/K is used in this study as described by Sauerland et al. [16], which results in flow occurring up the temperature gradient. While this is not typical in pure metals, this type of flow is oftentimes observed when a surface-active element changes the surface tension from that of the pure base material. This is generally caused by interaction with the gas adjacent to the fluid surface and is attributed to the high oxygen affinity of Ti. Flow of the material is confined to that material that experiences temperature above the melting temperature by controlling the viscosity of the material to be a function of temperature. The viscosity for solid is assumed to be 100 Pa·s and that for the liquid material is 0.01 Pa·s, which is sufficient to eliminate flow in the solid material. Simple diffusion-based mass transport is also included in this model with diffusion coefficients for the Ni, Ti, and Fe obtained as a function of temperature from the DICTRA MOBFE2 diffusivity database.

Phase prediction for the joints created through autogenous laser brazing was performed through Calculation of Phase Diagrams (CALPHAD) techniques. For an overview of the process used in this study, please refer to the authors' prior work [17]. Phase prediction was performed at various locations across the dissimilar metal interface. As each point experiences a different thermal profile, thermal histories were obtained from identical points within the thermal simulation. Compositional information was obtained through experimental analyses by EDS at these same locations. The phases predicted to form at these compositions, under the simulated thermal histories, are calculated using the CALPHAD

approach. This allows for quasi-spatially resolved data to be obtained.

**Phase Identification.** Due to the number of elements included in the combination between NiTi and SS, the high cooling rate obtained by the process, as well as the variable proportion of these elements across the autogenous laser brazed joint, phase identification at the interface requires a robust, multifaceted approach. This is achieved through a combined EDS and EBSD experimental measurement. The use of multiple characterization methods allows for significantly more accurate identification of unknown phases in nonequilibrium, multicomponent systems. EBSD is able to differentiate between different phases due to their different crystal structures; however, due to the numerous phases that could potentially be formed in NiTi–SS mixture, precise identification is difficult as there are a number of phases with identical space groups. While the Kikuchi patterns will vary slightly between these phases due to their different lattice spacing, these differences are often small and, by themselves, may result in the misidentification of phases. Further differentiation between phases can be obtained by characterizing the composition of each region and determining upper and lower-limits for the composition of each potential phase. This can be performed to clearly differentiate between phases such as TiFe<sub>2</sub> and Ni<sub>3</sub>Ti which both have a P6<sub>3</sub>/mmc space group but significantly different composition ranges. By doing so, the combined EBSD/EDS process is able to identify phases with much greater accuracy than either process alone.

The initial phase identification is performed directly by EBSD through a voting algorithm based on the Hough peak fit between the observed pattern and the theoretical position for a variety of Ni-, Ti-, and Fe-containing phases. Initial scans were performed with all of the phases observed in the ternary Ni–Ti–Fe equilibrium phase diagram included [18]. The potential phase solution list thus contained Ti<sub>2</sub>Ni, TiFe<sub>2</sub>, TiNi<sub>3</sub>, Ni<sub>4</sub>Ti<sub>3</sub>, NiTi, FeTi, FeNi<sub>3</sub>, FeNi, and SS 304 in place of  $\alpha$ -Fe. Each point in the two-dimensional EBSD map is linked to a specific phase through the voting scheme based on the experimental electron backscatter pattern having the closest fit to the theoretical pattern. An EDS map with the same spatial resolution is performed concurrently with the EBSD scan. The amounts of the three main elements, Ni, Ti, and Fe, are chosen to represent the composition. After the initial EBSD scan, the scan is rerun using the saved Hough peak locations from each point combined with the EDS map composition data. The addition of the composition data allows the voting algorithm to exclude phases from consideration, which have significantly different compositions than observed at the point in question. This is performed on a point-by-point basis resulting in a refined phase identification map.

The resultant EBSD maps are further refined by elimination of phases that are observed at very low amounts and in locations where their formation is unlikely, such as the identification of mixed phases within the base material far from the interface. This refinement is user-defined and typically results in phases which are observed in less than 0.1% of the two-dimensional scan area to be removed. These phases are generally only observed at single points, surrounded by phases identified as having the same space group.

## Experimental Setup

NiTi and stainless steel 316L wires, roughly 380 and 368  $\mu$ m in diameter, respectively, were cut to 7 in. lengths from spools. One end of each wire was ground flat with the surface perpendicular to the axis of the wire using 800 grit silicon carbide paper. Wires were cleaned in an ultrasonic bath of acetone for 15 min prior to assembly in a welding fixture. The welding fixture consisted of a pair of coaxial microchucks, one holding a SS tube slightly larger than the diameter of the wires. The wire sample to be irradiated by the laser was placed in the tube and allowed to protrude

roughly 5 mm from the end with the ground end facing the adjacent chuck. The second wire was fixed in the other chuck with its ground end facing the end of the tube. The ground faces of the samples were held together using an axial force applied by a spring on the wire to be irradiated. The axial force on the wires was set to 0.15 N by adjusting the compressed length of the spring.

Irradiation along the NiTi wires was performed using a continuous wave fiber laser operating at a wavelength of 1064 nm. The Gaussian spot was controlled to be the same size as the diameter of the wires. Laser power was adjusted up to a maximum of 9 W while scan speed was adjusted between 1.5 and 2.5 mm/s. The length of the scan was held constant at 2.5 mm. The laser irradiation was stopped 100  $\mu\text{m}$  from the joint interface in order to minimize unnecessary heating of the unirradiated wire. The sample was accelerated to the preset scan speed prior to laser irradiation and deceleration occurred after the conclusion of laser irradiation to ensure that sample translation occurred at a constant velocity during processing. Laser joining was performed in an inert environment of ultrahigh purity argon gas, which was flowed into the enclosed welding fixture at a flow rate of 10 cfh.

After joining the samples were tested in tension to fracture using a microtensile tester with bollard grips using a cross head speed of 0.5 mm/min. The gauge length was set at 100 mm. Fracture surface analysis was performed using a SEM while compositional analysis was performed using EDS. Phase identification was performed through the combined EDS/EBSD process discussed above.

## Results and Discussion

**Weld Geometry.** Figure 2 shows a typical joint created using the autogenous laser brazing process. This particular joint was formed using a laser power of 8.5 W directed toward the NiTi wire over a scan length of 2.5 mm at a scan speed of 1.75 mm/s. Overall, the joint shows a clean outward appearance with no obvious signs of porosity or cracking. The top surface of the irradiated NiTi wire shows a smooth, dark surface while the side and bottom of the wire experiences some roughening of the

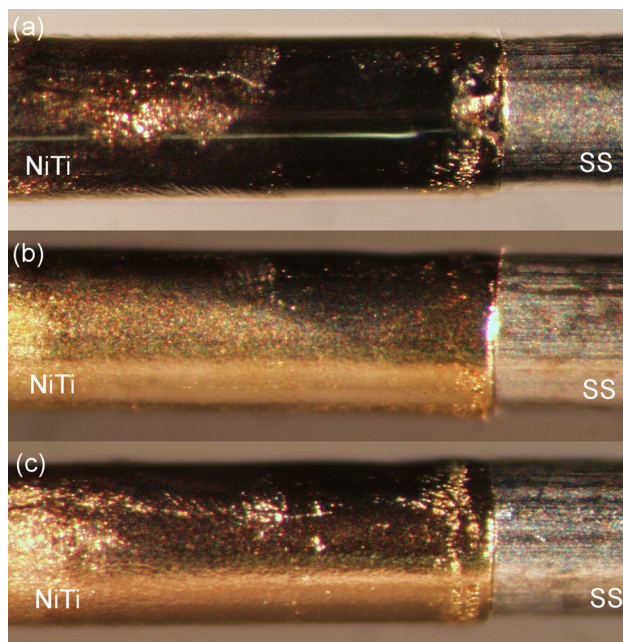


Fig. 2 Optical micrograph of dissimilar metal joint between NiTi and SS observed from the (a) top, (b) side, and (c) bottom of the joint. Sample irradiated on NiTi-side of joint. Note complete joining around circumference of wires.

surface. No large-scale deformation of the wire is observed indicating that significant melting of the base materials did not occur during processing. Minimal bulging is observed very close to the joint interface likely due to the softening of the NiTi as it is heated and the axial force applied on the irradiated wire. This deformation indicates that some softening of the material did occur and that the two wires were forced into contact. This is critical for the proposed autogenous laser brazing process since the greater interface conductance caused by the deformation will help to limit the temperature increase at the interface and keep the laser from over melting the wire. In contrast to the irradiated, NiTi, side of the joint, the SS side shows no signs of deformation or surface roughening. This indicates that the temperature on that side of the joint was maintained below the melting temperature. Oxidation of the NiTi wire surface is minimal, showing a nearly uniform, light straw color. No oxidation of the SS wire surface is observed.

Figure 3 is an optical micrograph of the same sample shown in Fig. 2 after cross sectioning along the Y-Z plane. A clean interface is observed with no porosity, cracking, or signs of incomplete joining at the interface. The joint itself is widest at the upper, irradiated surface of the wire and becomes narrower further from that surface. The increased width toward the top of the joint is likely due to the increased heat flux experienced by the top surface from direct laser irradiation which causes excess melting to occur. A faint outline of the melted portion of the NiTi wire, which has a slightly different veinlike morphology indicative of directional solidification, can be seen extending roughly 50  $\mu\text{m}$  below the irradiated surface. Regions of the joint opposite the irradiated surface show less evidence of growth direction. The mechanisms of joint formation in these two regions will be discussed further in the Compositional Analysis section.

**Compositional Analysis.** Quantitative EDS profiles performed across the NiTi-SS interface at different depths from the irradiated surface are shown in Figs. 4(a)-4(c). Each profile shows a constant composition of primarily Fe in the SS and a slightly Ni-rich composition in the NiTi side of the joint. Between the two

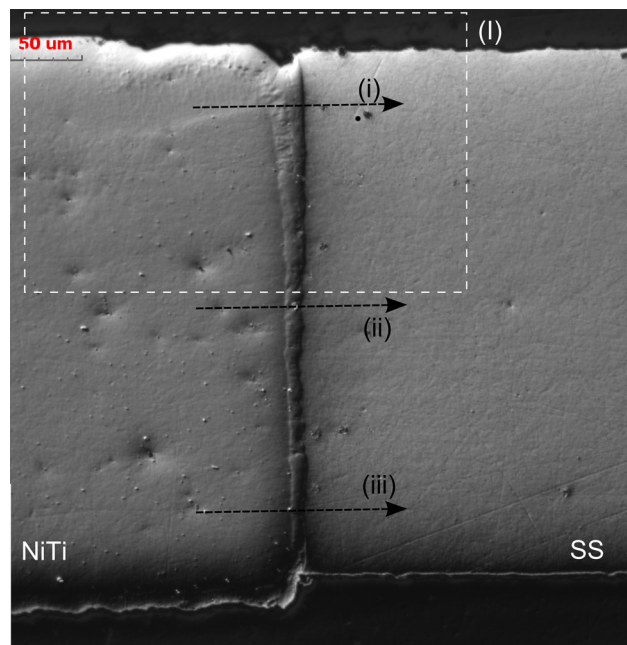
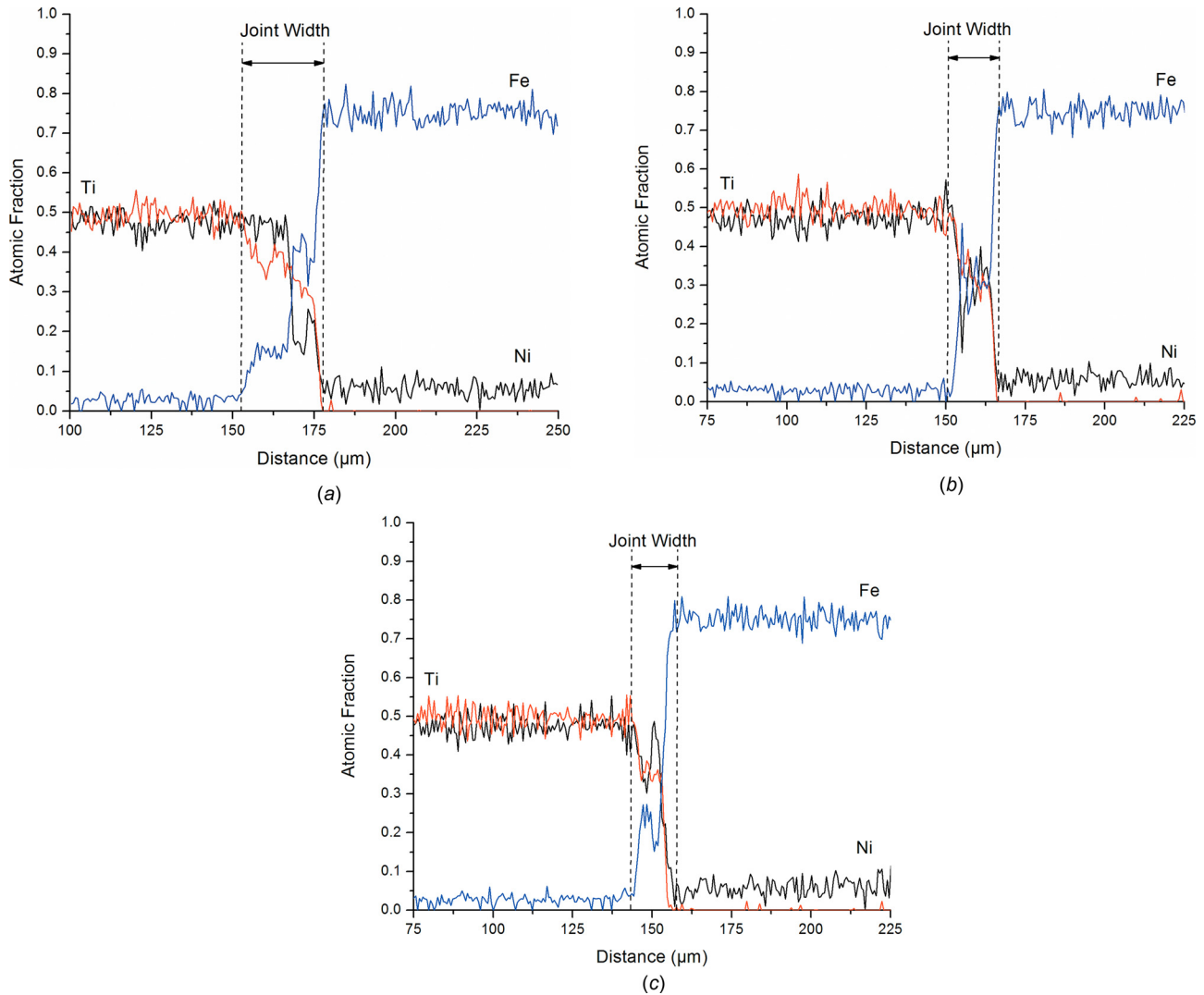
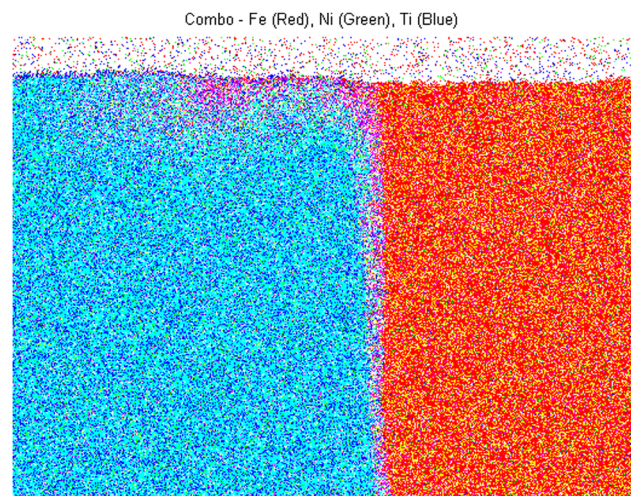


Fig. 3 Optical micrograph of joint cross section along the YZ-plane. Note wider joint width at top, irradiated surface and nearly uniform joint width along the remainder of the joint. Evidence of directional solidification is also observed in the top portion of the joint.



**Fig. 4** EDX line scan composition profiles for scans: (a) i, (b) ii, and (c) iii from Fig. 3. Note change in width of mixed zone (joint width) at different locations along wire thickness.

base metal compositions is the joined region showing a mixture between Fe, Ni, and Ti in varying proportions. The extent of this mixed region indicates the width of the joint. The uppermost EDS profile (Fig. 5(a)) shows a joint that is roughly 25  $\mu\text{m}$  wide. A steep dropoff in the iron composition, from roughly 75 at. % Fe to 4 at. % Fe, is observed at the same location at which the Ni and Ti compositions increase significantly; however, an appreciable amount of Fe is observed to exist roughly 25  $\mu\text{m}$  into the NiTi side of the joint. The second EDS profile (Fig. 5(b)), performed 125  $\mu\text{m}$  below the first, shows similar characteristics but with the mixed composition region extending only 15  $\mu\text{m}$  from the interface. The third EDS profile (Fig. 5(c)), performed 250  $\mu\text{m}$  below the first, shows a mixed region between the two base materials of a similar thickness. The variation in the composition profiles suggests that different joining mechanisms are dominant along different regions of the joint. Toward the laser irradiated surface the melted layer thickness is greater, which indicates a longer melt duration, allowing greater dilution of the SS into the molten NiTi. Toward the center of the wires, where minimal mixing of the two materials is observed, the melt layer thickness should be significantly smaller. The composition profile in this region resembles more of a diffusion-controlled process while the upper layers resemble more of a fusion-based joining mechanism. Figure 5 shows an EDS map of region I in Fig. 3. A clear delineation between the two materials is observed with a small layer of



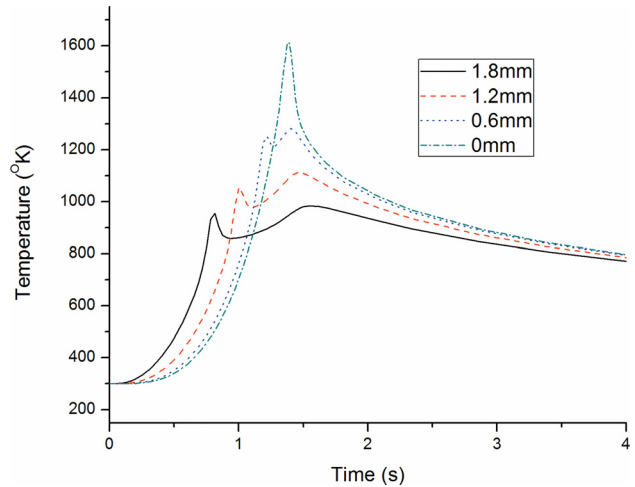
**Fig. 5** EDS Map of region 1 in Fig. 3 with the left side showing the composition of NiTi and the right showing the composition of Stainless Steel. Note transport of Fe-rich material along NiTi wire surface.

mixing between the two. The darker blue layer on the top of the NiTi wire is nearly all Ti and is likely a Titanium oxide. Ti-oxides are expected to form preferentially in these joints due to Titanium's high oxygen affinity.

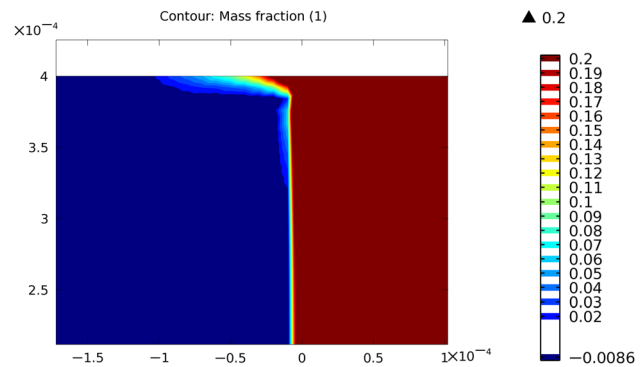
Thermal and compositional modeling of the autogenous laser brazing process is performed to understand the resultant composition profile at the interface. Figure 6 shows temperature contours in a joint pair with the laser directed at the NiTi wire at a number of different times. Figure 6(a) shows the steady-state temperature distribution around the laser spot far from the wire-wire interface. Thermal accumulation, as evidenced by the increase in peak temperature, is observed as the laser beam approaches the interface in Figs. 6(b) and 6(c). Some nonuniformity of the temperature at the joint is observed in the thermal model as the laser approaches the interface with the upper region showing a higher temperature consistent with the wider joint observed experimentally toward the top of the wire. Temperature-time profiles at various distances from the interface are shown in Fig. 7. The peak temperature of each point is seen to be a decreasing function of its distance from the joint interface with the facing surface of the joint experiencing the highest temperature rise. This is attributed to the thermal accumulation at the joint due to the imperfect conduction across the interface.

Figure 8 shows the resultant composition profile of a NiTi-SS joint as predicted by the combined heat transfer and fluid flow numerical simulation for the same laser parameters along the upper portion of the joint as shown in Fig. 5. The coloring is based on the RGB scale with red, green, and blue representing Fe, Ni, and Ti, respectively. The laser flux was applied to the top surface of the modeled geometry. A mixed zone is observed which is largest in width toward the irradiated surface and extends along the NiTi wire surface away from the joint. This is in good agreement with the experimentally observed profile shown in Fig. 5. This confirms that the positive sign for the surface tension coefficient is correct for the parameters and environment surrounding the NiTi wire during irradiation in autogenous laser brazing. This flow of SS material is caused by Marangoni convection which pulls the molten material along the surface of the NiTi wire toward the laser spot which is located to the left of the joint interface. No significant melting is observed in the lower portion of the joint in the simulation. This morphology is also in good agreement with the shape observed experimentally.

**Joint Width.** Figure 9(a) shows the width of joints produced through the autogenous laser brazing process as a function of laser power. While the joint widths at the center and bottom of the wires are nearly constant with laser power, the joint width at the top, irradiated portion of the wire is greater at the lowest and highest laser powers tested. This profile can be explained in terms of the thermal profile experienced by the wires at these different



**Fig. 7** Simulated temperature-time profiles for points at different distances from the joint interface. Note higher peak temperatures for points located closer to the interface indicating thermal accumulation.



**Fig. 8** Color contour map of mass fraction of Fe in NiTi-Fe joint formed by autogenous laser brazing as predicted by numerical simulation. Fluid flow is driven by Marangoni convection with a positive surface tension temperature coefficient. Resultant composition profile matches that observed experimentally as shown in Fig. 5. Right side shows pure Fe, left side shows NiTi, and gradient at upper surface shows mixing of materials due to Marangoni convection.

laser powers. For each of these samples, the laser scan speed is held at a constant 2 mm/s over the same 2.5 mm scan length. Thus, varying the laser power results in a change in total energy

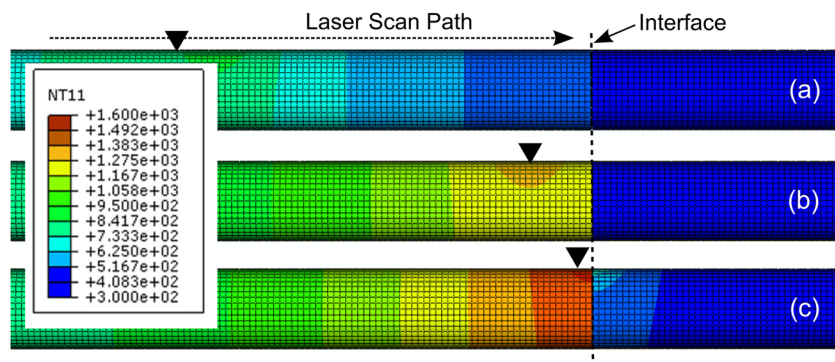


**Fig. 6** Thermal model of autogenous laser brazing process showing thermal accumulation at joint interface as laser beam approaches. “▼” symbol indicates position of laser beam. (a) Equilibrium temperature distribution far from interface. (b) Beginning of thermal accumulation at interface. (c) Melting of interface.

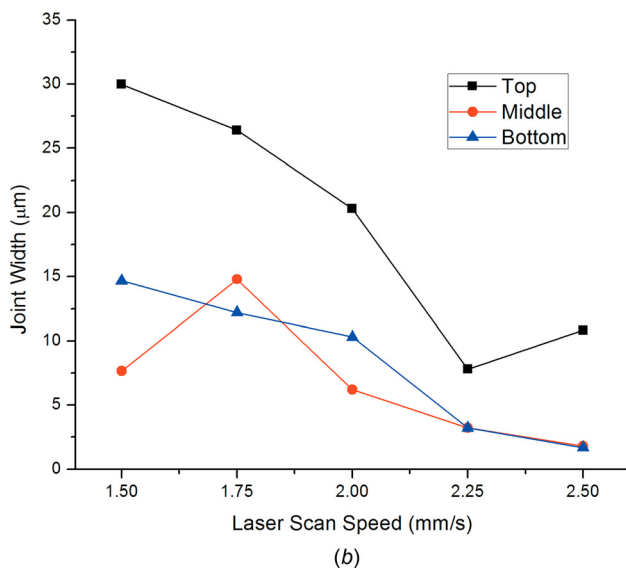
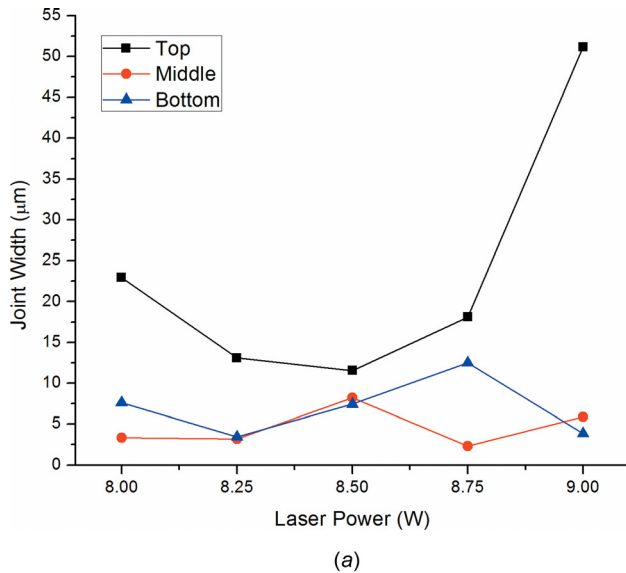


**Fig. 9 (a) Representative joint width versus laser power at constant scan speed. (b) Representative joint width versus scan speed at constant laser power. Note excessive melting of the top of the joint in (a) at extreme power levels due to different total energy input and thermal profile.**

input to the system while maintaining the total temporal shape of the irradiation. At low power levels, insufficient heating of the part leads to nonuniform melting at the interface and thus nonuniform heat conduction between the two wire faces. The majority of the joining occurs at the irradiated surface causing the high joint width. At the highest power level, excess heating of the irradiated wire occurs, resulting in overmelting and excessive mixing of the dissimilar materials leading to the high joint width. At the 8.5 W power level, it is observed that the joint width at all three depths is nearly the same. This is the preferred result to create the most uniform joint. It will also be shown that this is also the strongest configuration.

Figure 9(b) shows the width of the joints at three locations on the joint cross section as a function of scan speed as determined through EDS line profiles. The joint width can be seen to decrease as a function of scan speed. Similarly, this is attributed to the decrease in energy put into the wires by the faster laser scan at constant laser power. The discrepancy between the joint widths toward the laser irradiated surface (denoted top in the figure) and the opposite surface (bottom) also tends to decrease with

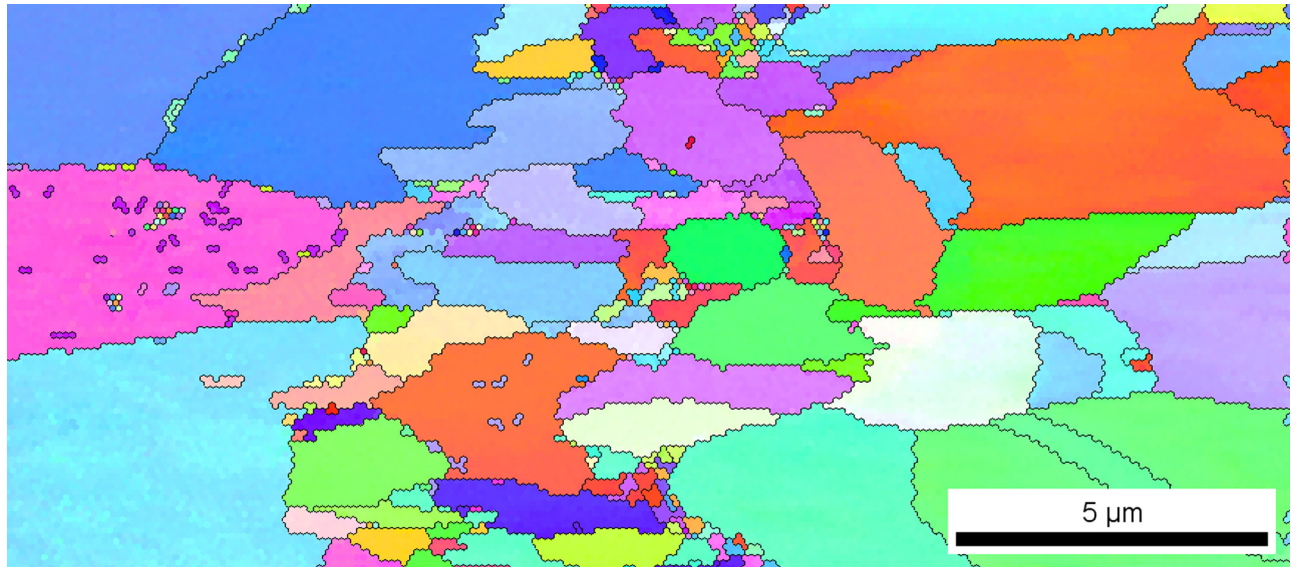
increasing scan speed. Each sample in Fig. 9(b) was irradiated with a constant laser power of 8.5 W and thus, decreasing the scan speed results in increased input power into the wire samples. This results in overheating of the irradiated wire and significant deformation at the joint interface. Excessive melting is observed along the entire surface of the wire due to the limited conduction pathways which results in the large top and bottom joint widths. At the other extreme with a scan speed of 2.5 mm/s, the heating becomes excessively localized to the upper portion of the joint due to the limited interaction time of the laser with each point. This time becomes less than the characteristic time for heat conduction across the wire diameter, resulting in a further decrease in the middle and bottom joint widths while the top joint widths starts to increase.

Figure 9 also shows that the joint width is significantly smaller than the beam spot size for all processing conditions. During processing the laser beam is defocused such that the spot size on the sample surface is roughly 400 μm. The largest joint width in Fig. 10 is just over 50 μm while the smallest is only 2 μm. In either case, the joint width is much smaller than the irradiating beam size. This would not be possible if the laser beam were to directly melt the material under it. Rather, this suggests that localized melting is occurring at the interface due to the limited heat conduction capability across the interface prior to joining. This provides further evidence suggesting that heat accumulation at the interface is responsible for the localized melting and joining which also leads to minimal mixing between the dissimilar metals.

While the joint width is significantly smaller than the laser beam spot size, it is likely that if the melt pool is able to become large enough or exist for an extended amount of time, convection of the molten metal within the joints may occur due to Marangoni forces resulting in additional mixing and dilution of the base materials. In addition, if the laser scan is performed too slowly, the interface will experience significant preheating long before the laser is able to reach the interface and melt the material which will result in unnecessary diffusion between the materials. Due to the axial force exerted on the wires, extended periods at elevated temperatures may also lead to deformation of the base materials and reduction of the contact resistance at the dissimilar metal interface even in the solid state. This would limit the amount of thermal accumulation possible at the interface and may result in incomplete joining.

**Phase Identification.** Figure 10 shows an EBSD map of a small region on a cross section along the YZ-plane of a sample joined through autogenous laser brazing. Grains are identified as contiguous regions with similar color based on the Euler angle coloring while grain boundaries are added to locations where adjacent points have a >5 deg orientation difference. The left side of the image consists of NiTi base metal while the right side of the image is SS. Between them is a layer of small grains, which represents the mixed interface between the two base metals. The grains are observed to be roughly equiaxed with some grain in the joint showing some directionality along the length of the wires or across the joint. In general, the NiTi grains on the right are observed to be larger than those in the SS. No significant orientation relationship is observed between the base metal grains and the adjacent grains in the joint, which suggests that they did not grow from the original base materials.

A phase map of the same region shown in Fig. 10 is shown in Fig. 11. The phases were identified using the combined EBSD/EDS process described in the background section of this work. As noted above, the left- and right-most sides of the region are identified as NiTi and SS, respectively. The joint itself, is identified as a mix of TiFe<sub>2</sub>, a Laves-type phase, TiNi<sub>3</sub>, and FeTi. The TiFe<sub>2</sub> and TiNi<sub>3</sub> represent the majority of the joint while the FeTi is observed as a thin layer along the Ni–Ti joint interface. The TiFe<sub>2</sub> and TiNi<sub>3</sub> are also thoroughly mixed within the joint, showing no



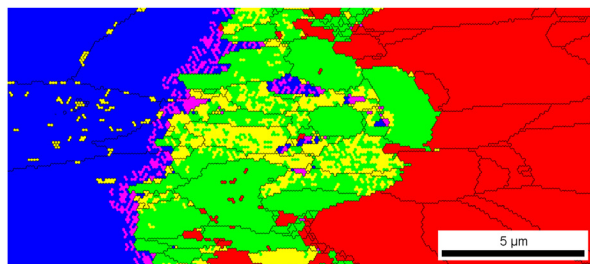
**Fig. 10** EBSD map of interface on YZ-plane cross section of sample joined at 8.5 W and 1.75 mm/s scan speed. Note large grains on left and right and a layer of smaller grains at the center. Coloring is based on Euler angles with red, green, and blue representing the (001), (101), and (111) normal orientations for cubic crystals and the (0001), (2110), and (1010) normal orientations for hexagonal crystals. No specific orientation relationship is observed between the base metal grains and those within the joint. Color image available when viewed online.

specific spatial relationship. This is expected to be due to the fluid flow occurring within the joint during processing caused by the combination of Marangoni convection and wetting-induced flow along the interface. The thin, nearly uniform width FeTi layer is considered to be caused by diffusion of Fe into the NiTi matrix. FeTi and NiTi have identical space groups and the transformation from NiTi to FeTi requires only a substitution of a Fe atom for a Ni. This excess Ni can then be used to form the TiNi<sub>3</sub> in the joint itself. The two phases observed in the joint, TiNi<sub>3</sub> and TiFe<sub>2</sub>, also have the same space group but require more than a substitution of atoms to change between them. The fact that the two phases are seen to exist even within the same grain suggests that maintaining the same orientation between them is the energetically favorable configuration. The existence of isolated FeTi/NiTi and SS grains within the joint region provides further evidence which indicates the existence of significant fluid flow during the autogenous laser brazing process between the two wires.

Figures 12(a) and 12(b) show phase development curves as predicted by the CALPHAD approach described in the background section of this work for two different interface compositions. The composition simulated in Fig. 12(a) is 48 at. % Ni, 37 at. % Ti, 14 at. % Fe, and 1 at. % Cr, which is observed to exist in the upper portion of the joint toward the irradiated surface, closer to the NiTi base material. The CALPHAD simulation predicts the initial formation of TiFe<sub>2</sub> from the melt as it is cooled followed by the formation of Ni<sub>3</sub>Ti prior to full solidification. Figure 12(b) shows the predicted phase formation for a composition of 34 at. % Ni,

35 at. % Ti, 23 at. % Fe, and 8 at. % Cr, which is observed throughout the joint closer to the SS base material. Similar to Fig. 12(a), TiFe<sub>2</sub> is predicted to form first, albeit at a slightly higher temperature. The Ni<sub>3</sub>Ti phase also is predicted to form but result in a significantly smaller mole-fraction by the end of solidification due to the extended time for TiFe<sub>2</sub> formation. In both cases, the two phases that are formed first from the melt are TiFe<sub>2</sub> and TiNi<sub>3</sub>. This is in good agreement with the phase identification performed by EBSD above. The EBSD phase map in Fig. 11 also shows that the region has a greater area fraction of TiFe<sub>2</sub> (22.9%) compared to Ni<sub>3</sub>Ti (8.7%). This measurement, which was performed toward the center of the joined wires, also follows the trend predicted by the CALPHAD simulation. It is interesting to note, however, that the formation of FeTi at the NiTi-side of the interface was not predicted by the model. This is due to the assumption of a homogenous composition made by the simulation. The TiFe forms at a location where there is a significant compositional gradient from the mixed joint region to the NiTi base material. At the compositions simulated in Fig. 12 no FeTi is predicted to form.

**Joint Strength.** An ideal joint between dissimilar materials will have a strength that exceeds the weaker of the base materials. Figure 13 shows the load-displacement curves for the NiTi and SS wires in the as-received condition. The SS wire yields at an applied load of roughly 30 N and fractures at a load of nearly 60 N after significant plastic deformation. The NiTi sample initially



Phase	Total Fraction	Partition Fraction
Stainless Steel 304	0.391	0.391
TiFe <sub>2</sub>	0.229	0.229
TiNi <sub>3</sub>	0.087	0.087
NiTi Austenite	0.271	0.271
FeTi	0.022	0.022

**Fig. 11** EBSD/EDS phase identification map of region shown in Fig. 11. Joint interface is roughly 5 μm in width and consists of primarily TiFe<sub>2</sub> and TiNi<sub>3</sub>. Note layer of FeTi at NiTi-interface boundary.

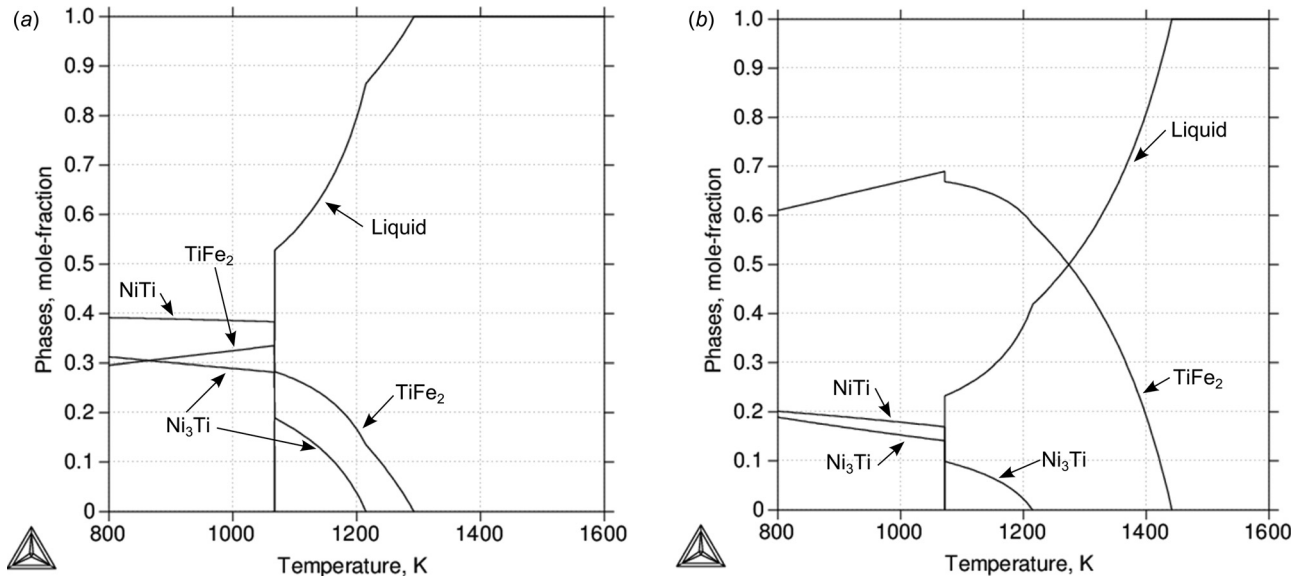


**Fig. 12** Phase development curves as predicted by CALPHAD simulation for compositions of (a) 48 at. % Ni, 37 at. % Ti, 14 at. % Fe, 1 at. % Cr and (b) 34 at. % Ni, 35 at. % Ti, 23 at. % Fe, and 8 at. % Cr. Note initial formation of TiFe<sub>2</sub> from liquid in both cases followed by formation of Ni<sub>3</sub>Ti prior to complete solidification.

deforms elastically until the phase transformation from austenite to martensite occurs at about 50 N of applied load. A load plateau is observed at this point as the deformation of the material is accommodated through the phase transformation. After the load plateau another linear elastic region is observed and fracture is observed at nearly 160 N of applied load. This load-displacement profile is indicative of the superelastic effect. In a real-world application that requires a joint between these two materials it is likely that the NiTi composition would be adjusted such that the phase transformation occurred before any plastic deformation would be observed in the SS.

Figure 14 shows a typical load-displacement curve for a sample formed using autogenous laser brazing. The initial low-slope region is caused by slack in the wire gripping Bollard apparatus used for the tensile testing. Once the wire is taught, the load-displacement curve shows the typical elastic portion, which is a combination of elastic deformation of the NiTi and SS wires, followed by yield at roughly 38 N of load, and an extended period of plastic deformation of the joined sample to a total elongation of

roughly 6 mm when fracture occurs. As shown in Fig. 14, the yield stress of the SS is below both the phase transformation and fracture stresses of the base NiTi wire. Thus, the plastic deformation observed in the joined sample occurs within the SS side of the joint and no permanent deformation of the NiTi is observed.

The occurrence of fracture in the joined samples at very similar levels of load that induce the austenite-to-martensite phase transformation in the base NiTi wires does suggest the possibility of the phase transformation itself contributing to the failure. Due to the change in material properties across the joint, there exists a stress concentration at the dissimilar metal interface. As the joined wires are loaded in tension, both wires start deforming elastically,

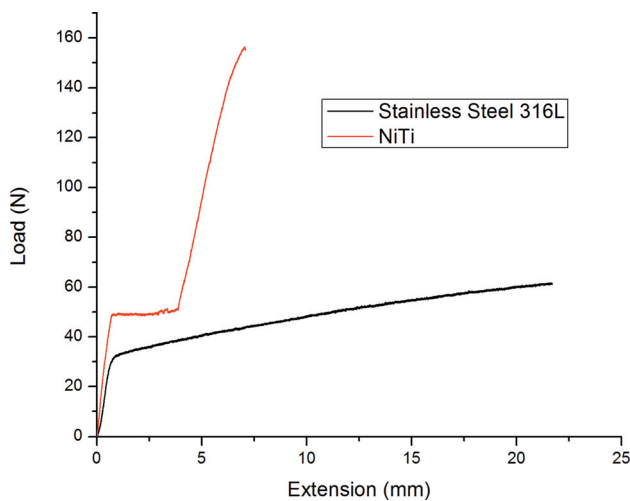


**Fig. 13** Load-displacement curves for base materials NiTi and SS. Note load plateau in NiTi curve indicating phase transformation accommodated deformation (i.e., superelasticity).

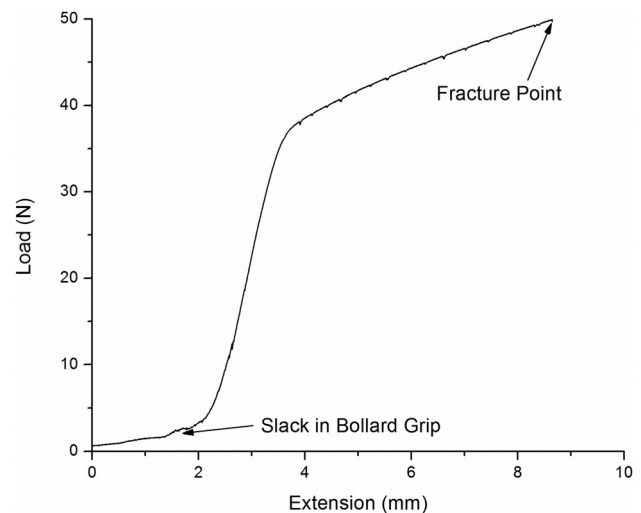


**Fig. 14** Typical load-displacement curve for joint formed using autogenous laser brazing process. Appreciable plastic deformation is observed after yield, which occurs at the same load observed in the base SS material as shown in Fig. 13. Total plastic extension is lower than observed in the original base material but is for a shorter length of SS wire. Note initial shallow slope region due to straightening of the wire by the Bollard gripping apparatus.

followed by plastic deformation of the SS. When the load required to induce the phase transformation in the NiTi is reached, the material will undergo the martensitic phase transformation, which includes a diffusionless, shear-type deformation of the existing austenitic lattice to form twinned martensite. Additional loading will cause the twinned martensite to detwin to accommodate the deformation without fracture. Unlike the elastic deformation occurring within the NiTi up to this point, however, the martensitic phase transformation is anisotropic at the grain-level. At the interface, these anisotropic grains are in contact with more isotropically deforming materials such as FeTi, TiFe<sub>2</sub>, and Ni<sub>3</sub>Ti. NiTi grains with unfavorable orientations relative to the applied load will not as easily accommodate additional deformation through the martensitic transformation and detwinning of the martensite causing additional stress concentrations. This is considered to be a potential reason for the failure to occur at the martensitic transformation load. Further study is required to elucidate the true relationship at the interface between the shape memory material and the adjacent elastic-plastic material during the phase transformation.

*Effect of Laser Power.* The effect of laser power on the strength of joints formed using the autogenous laser brazing process is shown in Fig. 15. The tensile load required to fracture the joints, which were formed at a constant laser scan speed of 2 mm/s, reaches a maximum at a power level of 8.5 W. Both higher and lower power levels result in reduced load carrying capability as well as higher variability between samples. Besides the peak at 8.5 W, the overall trend in strength of the joints is to increase with laser power. The reason for this is shown in Fig. 16, which depicts the fraction of the fracture surfaces that were observed to have been joined prior to failure on both the NiTi and SS sides of the joint. The profile with laser power depicted in Fig. 16 has a strong resemblance to that shown in Fig. 15, the load at fracture of the joints. While slightly less pronounced, there exists a peak at the 8.5 W power level and the variability in the area fraction is also minimized at this point. As described above, the joints with the highest strength are also those which showed the smallest, most uniform joint thicknesses as depicted in Fig. 9(a). As shown through EBSD/EDS measurements above, the formation of brittle intermetallics at the interface cannot be eliminated. Their thickness, however, does have an appreciable effect on their strength due to the maximum crack size that can exist within the brittle layer. As the joints get smaller and more uniform, the maximum crack size decreases, increasing the joints resistance to fracture.

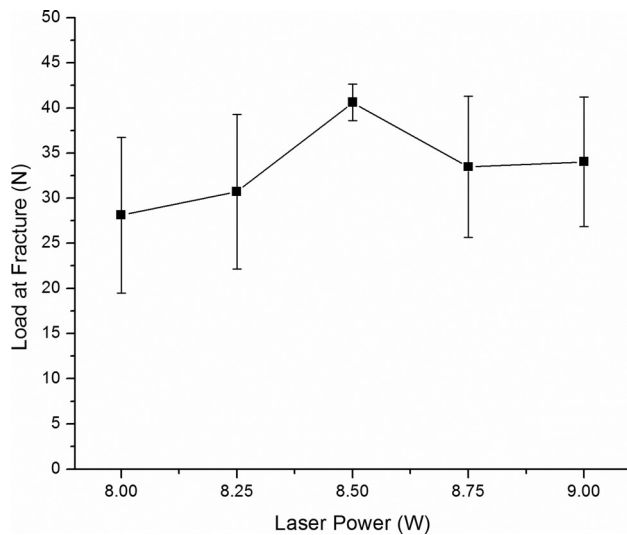


Fig. 15 Load at fracture as a function of laser power at constant scan speed. Peak load is observed at same laser power that results in most uniform joint width (Fig. 9(a)).

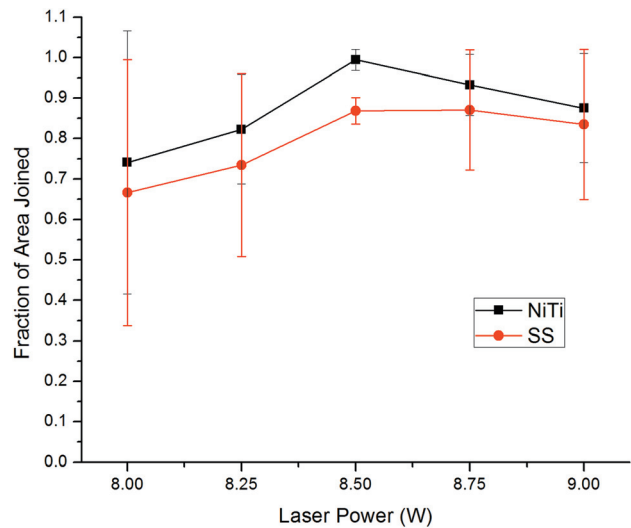


Fig. 16 Fraction of cross-sectional area joined versus laser power for samples joined at a scan speed of 2 mm/s. Note close resemblance to joint strengths shown in Fig. 15 both in magnitude and standard deviation.

*Effect of Scan Speed.* Figure 17 shows a downward trend in the strength of the joined samples with increasing scan speed. As the laser scan speed is increased the overall energy input into the wire is reduced due to the constant applied power of 8.5 W. As discussed above, this can have the effect of decreasing the melt layer size or eliminating the melt layer all together. As scan speed is increased, the uniformity of temperature at the interface is also reduced which can result in insufficient melting to cover the entire faying surfaces resulting in decreased strength. At the lowest scan speed of 1.5 mm/s, the strength shows some variation but the average value is nearly the same as the peak strength observed, which occurs at a scan speed of 1.75 mm/s. At this slightly higher speed, there is nearly no variation in strength between samples. Strengths drop off steadily as the scan speed is further increased. This reason for this profile is explained by Fig. 18, which shows the fraction of the cross-sectional area that was joined prior to fracture as a function of scan speed. A similar trend to that observed for the strength is shown. The joined area fraction is

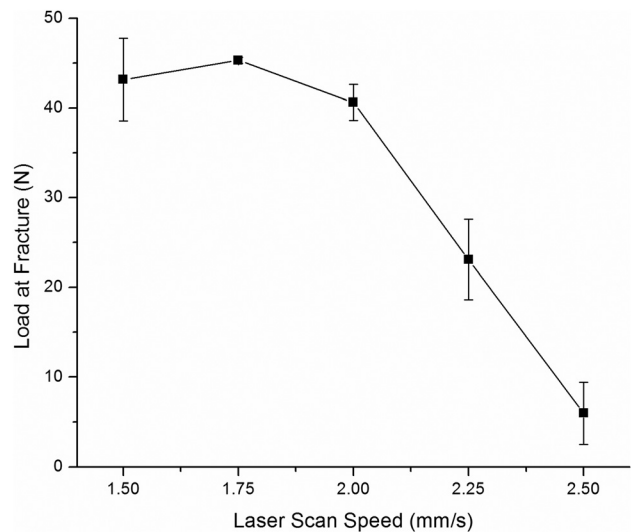
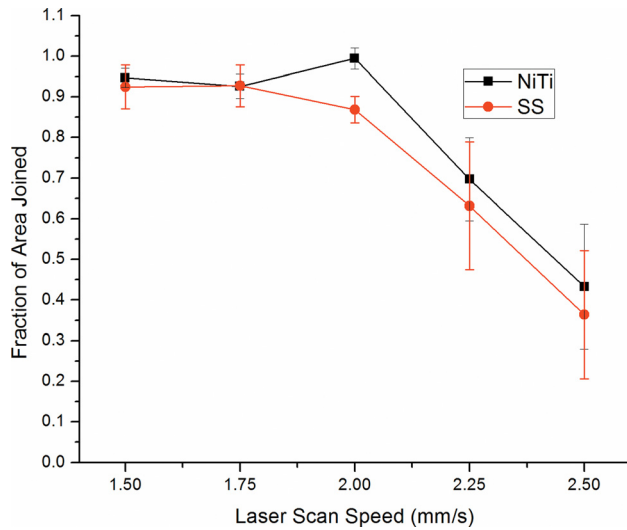


Fig. 17 Load at fracture as a function of scan speed for a constant laser power. Decreasing trend caused by lower energy input at higher scan speeds.

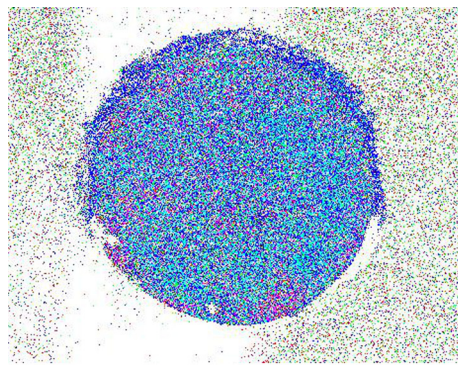


**Fig. 18** Fraction of wire cross-sectional area joined at interface as a function of laser scan speed for samples irradiated with 8.5 W laser power. Note close resemblance to load at fracture profile as a function of scan speed shown in Fig. 17.

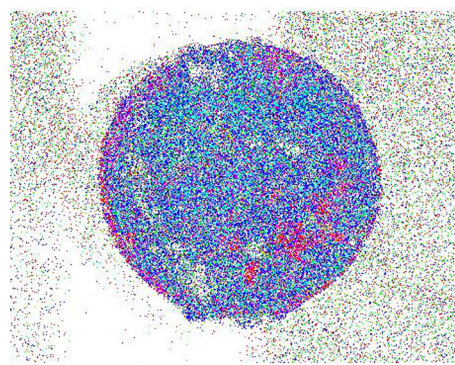
seen to drop off rapidly above a laser scan speed of 2 mm/s. Thus, the decrease in load at fracture with scan speed is caused by the insufficient joining at the interface due to insufficient melt volume or excessive localization of the thermal input.

Both sets of experiments, those with varied scan speed and those with varied laser power, suggest that optimal strength is achieved for joints which cover the surface area of the wire ends while maintaining minimal, uniform joint width across the wire diameter. As the joint itself consists of primarily  $\text{TiFe}_2$  and  $\text{Ni}_3\text{Ti}$ , both of which are brittle intermetallics, minimizing the width of the joint is crucial so as to take advantage of a smaller initial crack size which leads to a greater stress for brittle fracture along the intermetallic layer.

**Fracture Surface Analysis.** Figures 19(a) and 19(b) show compositional maps over the fracture surfaces of a joint created using the autogenous laser brazing process. The maps for each element have been combined into a RGB color scheme where the intensity of each color represents the signal intensity captured by the EDS for each pixel where red, green, and blue stand for Fe, Ni, and Ti, respectively. Most of the fracture surface, on both the NiTi and SS sides of the joint, is dominated by green and blue, which indicates that fracture occurred in Ni- and Ti-rich regions



(a)



(b)

**Fig. 19** Representative EDS maps of fracture surfaces on (a) NiTi and (b) SS sides of joint. Red, green, and blue, represent Fe, Ni, and Ti. Majority of fracture surfaces show Ni- and Ti-rich composition with patches of Fe-rich areas.

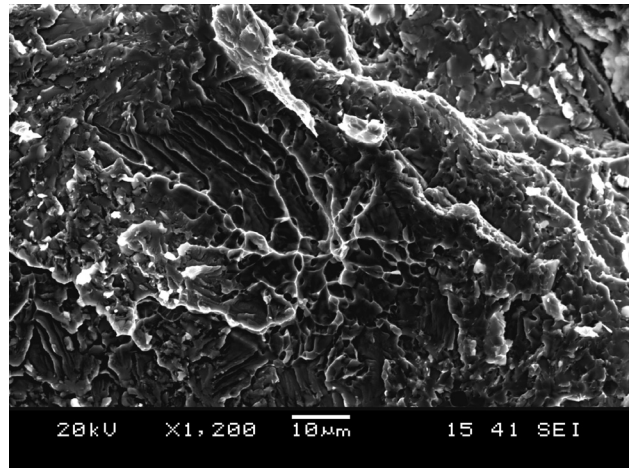


**Fig. 20** SEM of fracture surface for sample irradiated on SS suggesting quasi-cleavage fracture

of the joint. Quantitative compositional analysis of these regions shows that they have a composition of 34.45 at. % Ni, 49.46 at. % Ti, 12.86 at. % Fe, and 3.23 at. % Cr on the NiTi fracture surface and 30.43 at. % Ni, 44.20 at. % Ti, 19.21 at. % Fe, and 6.17 at. % Cr on the SS fracture surface. Since these compositions are not the same as either base material it can be concluded that fracture is occurring in the joint itself rather than within one of the base materials. Regions with primarily red coloring indicate incomplete joining or fracture in the base SS wire.

The load-displacement curves for the two base materials shown in Fig. 13, along with electron micrographs of the associated fracture surfaces (not shown), confirms that the base materials fail through ductile fracture. While many of the joints produced using the new autogenous laser joining process have reached strengths above the yield strength of the SS, failure is always observed to occur at the joint rather than in the SS—base material during tensile testing. Figure 20 shows a typical fracture surface as seen through electron microscopy for a sample joined using the autogenous laser joining process. The surface has a morphology indicative of quasi-cleavage fracture, and as discussed above, fracture is believed to be occurring within the joint. While the effect of NiTi's superelastic phase transformation on the stress at the joint has yet to be determined, further improvements to autogenous laser brazing joints are expected to come through refinement of the laser scanning pattern, both in space and time, to provide the most uniform thermal profile at the joint and further reduce melt volume and material mixing.

## Conclusion

Autogenous laser brazing has been investigated for creating seamless joints between two biocompatible materials, NiTi and SS 316L for medical device applications. Joints formed using this method possess strengths which exceed the yield stress of the SS base material during tensile testing. EDS mapping of the joint cross sections indicated that joint widths were significantly smaller than the incident laser beam diameter while resultant strength measurements suggest that joint strength is closely tied to joint width and uniformity. Fluid flow within the melt pool is dominated by Marangoni convection with a positive surface energy-temperature coefficient. Combined EBSD/EDS maps at the interface identify the joint as consisting of a mixed TiFe<sub>2</sub> and Ni<sub>3</sub>Ti layer. The minimal joint widths achieved and the high joint strengths show the viability of autogenous laser brazing as a method for creating robust joints between the NiTi and SS biocompatible dissimilar material pair.

## References

- [1] Hilfiker, P. R., Quick, H. H., Schmidt, M., and Debatin, J. F., 1999, "In Vitro Image Characteristics of an Abdominal Aortic Stent Graft: CTA Versus 3D MRA," *Magma*, **8**(1), pp. 27–32.
- [2] Li, M. G., Sun, D. Q., Qiu, X. M., and Yin, S. Q., 2006, "Corrosion Behavior of the Laser-Brazed Joint of TiNi Shape Memory Alloy and Stainless Steel in Artificial Saliva," *Mater. Sci. Eng.: A*, **441**(1–2), pp. 271–277.
- [3] Ghosh, M., and Chatterjee, S., 2002, "Characterization of Transition Joints of Commercially Pure Titanium to 304 Stainless Steel," *Mater. Charact.*, **48**(5), pp. 393–399.
- [4] Kundu, S., Ghosh, M., Laik, A., Bhanumurthy, K., Kale, G., and Chatterjee, S., 2005, "Diffusion Bonding of Commercially Pure Titanium to 304 Stainless Steel Using Copper Interlayer," *Mater. Sci. Eng.: A*, **407**(1–2), pp. 154–160.
- [5] Kundu, S., and Chatterjee, S., 2008, "Characterization of Diffusion Bonded Joint Between Titanium and 304 Stainless Steel Using a Ni Interlayer," *Mater. Charact.*, **59**(5), pp. 631–637.
- [6] Bauer, I., Russek, U. A., Herfurth, H. J., Witte, R., Heinemann, S., Newaz, G., Mian, A., Georgiev, D., and Auner, G. W., 2004, "Laser Microjoining of Dissimilar and Biocompatible Materials," *Proc. SPIE*, **5339**, pp. 454–464.
- [7] Borrisutthekul, R., Yachi, T., Miyashita, Y., and Mutoh, Y., 2007, "Suppression of Intermetallic Reaction Layer Formation by Controlling Heat Flow in Dissimilar Joining of Steel and Aluminum Alloy," *Mater. Sci. Eng.: A*, **467**(1–2), pp. 108–113.
- [8] Louzguine, D. V., Kato, H., Louzguina, L. V., and Inoue, A., 2004, "High-Strength Binary Ti-Fe Bulk Alloys With Enhanced Ductility," *J. Mater. Res.*, **19**(12), pp. 3600–3606.
- [9] Ray, R., 1972, "The Constitution of Metastable Titanium-Rich Ti-Fe Alloys: An Order-Disorder Transition," *Metall. Trans.*, **126**(3), pp. 362–629.
- [10] Elmer, J. W., Palmer, T. A., Babu, S. S., Zhang, W., and DebRoy, T., 2004, "Phase Transformation Dynamics During Welding of Ti-6Al-4V," *J. Appl. Phys.*, **95**(12), pp. 8327–8339.
- [11] Elmer, J. W., and Palmer, T. A., 2006, "In-Situ Phase Mapping and Direct Observations of Phase Transformations During Arc Welding of 1045 Steel," *Metall. Mater. Trans. A*, **37A**(7), pp. 2171–2182.
- [12] Borrisutthekul, R., Miyashita, Y., and Mutoh, Y., 2005, "Dissimilar Material Laser Welding Between Magnesium Alloy AZ31B and Aluminum Alloy A5052-O," *Sci. Technol. Adv. Mater.*, **6**(2), pp. 199–204.
- [13] Lee, M. K., Lee, J. G., Choi, Y. H., Kim, D. W., Rhee, C. K., Lee, Y. B., and Hong, S. J., 2010, "Interlayer Engineering for Dissimilar Bonding of Titanium to Stainless Steel," *Mater. Lett.*, **64**(9), pp. 1105–1108.
- [14] Mys, I., and Schmidt, M., 2006, "Laser Micro Welding of Copper and Aluminum," *Proc. SPIE* **6107**, p. 610703.
- [15] Yao, C., Xu, B., Zhang, X., Huang, J., Fu, J., and Wu, Y., 2009, "Interface Microstructure and Mechanical Properties of Laser Welding Copper-Steel Dissimilar Joint," *Opt. Lasers Eng.*, **47**(7–8), pp. 807–814.
- [16] Sauerland, S., Lohöfer, G., and Egly, I., 1993, "Surface Tension Measurements on Levitated Liquid Metal Drops," *J. Non-Cryst. Solids*, **156–158**(Part 2), pp. 833–836.
- [17] Satoh, G., Yao, Y. L., and Qiu, C., 2012, "Strength and Microstructure of Laser Fusion-Welded Ti-SS Dissimilar Material Pair," *Int. J. Adv. Manuf. Technol.*, **66**(1–4), pp. 469–479.
- [18] Raghavan, V., 2010, "Fe-Ni-Ti (Iron-Nickel-Titanium)," *J. Phase Equilib. Diffus.*, **31**(2), pp. 186–189.